Delft University of Technology

Document Version
Final published version

Licence
Dutch Copyright Act (Article 25fa)

Citation (APA)
Spirito, M., & Martens, J. (2025). Advances in Hardware and Measurement Techniques to Enable Better Millimeter-Wave Device Characterization and Modeling. *IEEE Microwave Magazine*, *26*(4), 32-44.
https://doi.org/10.1109/MMM.2024.3524849

Important note
To cite this publication, please use the final published version (if applicable).
Please check the document version above.

Copyright
In case the licence states “Dutch Copyright Act (Article 25fa)”, this publication was made available Green Open Access via the TU Delft Institutional Repository pursuant to Dutch Copyright Act (Article 25fa, the Taverne amendment). This provision does not affect copyright ownership.
Unless copyright is transferred by contract or statute, it remains with the copyright holder.

Sharing and reuse
Other than for strictly personal use, it is not permitted to download, forward or distribute the text or part of it, without the consent of the author(s) and/or copyright holder(s), unless the work is under an open content license such as Creative Commons.

Takedown policy
Please contact us and provide details if you believe this document breaches copyrights.
We will remove access to the work immediately and investigate your claim.

This work is downloaded from Delft University of Technology.

Advances in Hardware and Measurement Techniques to Enable Better Millimeter-Wave Device Characterization and Modeling

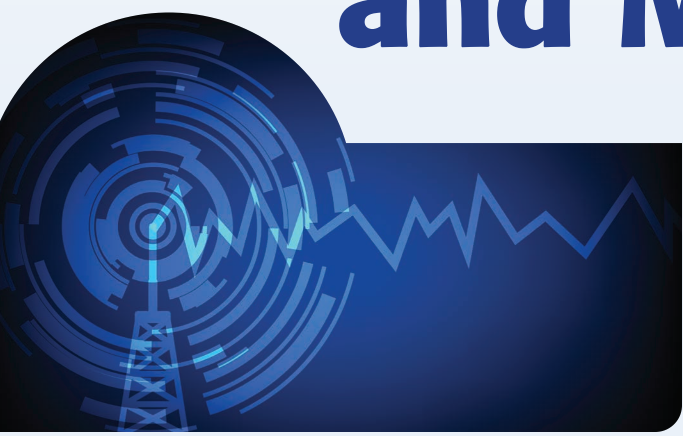

©SHUTTERSTOCK.COM/NATTHANICHA CHEENCHANYA

Marco Spirito and Jon Martens

Introduction

The discussion of millimeter-wave (mm-wave) applications above 110 GHz has been ubiquitous in recent years (e.g., [1], [2], [3], [4], and [5]), and measurements targeting the modeling of devices and subsystems for the aforementioned

Marco Spirito (m.spirito@tudelft.nl) is with Delft University of Technology, 2628 CD Delft, The Netherlands.
Jon Martens (jmartens@anritsu.com) is with Anritsu, Morgan Hill, CA 95037 USA.

Digital Object Identifier 10.1109/MMM.2024.3524849
Date of current version: 7 March 2025

1527-3342 © 2025 IEEE. All rights reserved, including rights for text and data mining, and training of artificial intelligence and similar technologies.

Authorized licensed use limited to: TU Delft Library. Downloaded on July 28,2026 at 14:04:21 UTC from IEEE Xplore. Restrictions apply.

frequency range have also received attention, as these are central to the design and validation processes (e.g., [6], [7], [8], [9], [10], [11], and [12]). In the past decade, the community has gone from coarse measurements with rather wide uncertainty bounds and relatively simple device models to structures that may be converging in completeness and complexity (if maybe not uncertainty) to those seen at lower frequencies. While the importance of the measurement core to validation and assessment is clear, that link to model development can be more nuanced, as simulations, low-frequency measurements, and other data play an increasingly important role. It can be argued that, at higher mm-wave frequencies, there is perhaps added importance to RF measurement data, due to an increase in the number of relevant mechanisms (e.g., parasitics that vary rapidly with frequency as well as frequency-dependent linearity terms) and their variability. These RF measurements must be acquired in a frequency range where power generation is difficult (i.e., the terahertz gap) and the receiver noise floors are elevated. In this article, we review the evolution of key measurement techniques and test benches that are required for device characterization (small-signal and first-order nonlinear regions) and model validation in the mm-wave bands above 110 GHz.

Many aspects of mm-wave measurement have been addressed in recent years, including 1) criticalities in on-wafer calibration (e.g., [13] and [14]), 2) the development of newer probe and interface structures for measurements (e.g., [15] and [16]), 3) mm-wave S-parameter measurements (e.g., [17]), 4) power measurements (e.g., [18]), 5) load pull (e.g., [19]), and many other topics. In most of these cases, there has been evidence of improvements in uncertainties and the understanding of sensitivities and mechanisms. Perhaps discussed less often thus far are key aspects of instrumentation for modeling and validation, particularly as there is movement to less-than-linear types of characterization, namely,

- *Absolute stimulus power delivered to the device under test and its accuracy*: This is not just to ensure linearity (in the case of small-signal measurements) or the desire for a specific level of device under test (DUT) nonlinearity but also to manage the signal-to-noise levels, as the noise floor may be limited at higher frequencies. The harmonic and spurious content of this signal may also be relevant, as is the dependence on the power level.
- *Receiver characteristics*: Obviously, the measurement noise floor is very relevant to the signal-to-noise ratio (SNR) calculations. In addition, the linearity of the measuring receivers is of interest as stimulus (and the DUT output) levels increase.

Perhaps more importantly, key questions are how all these measurement attributes affect models that may be extracted or performance that has to be verified and how these effects trend as one goes higher into the mm-wave spectrum. These hardware and system-centric attributes can vary significantly with different setup architectures. Thus, grand general conclusions may not be possible. Nevertheless, their trends and tendencies must be assessed for accurate and high-fidelity high-frequency measurements. One place to start is with a generalized network analysis-based test bench that could be used for mm-wave model development, as shown in Figure 1.

The generic diagram in Figure 1 applies to some of the commonly used broadband/mm-wave structures that include a base (microwave) vector network analyzer (VNA) and external modules that include multiplied source paths and harmonic converters. Many different external module designs exist (e.g., [20]), and only one such exemplary block diagram is shown in Figure 1. The source multiplication adds some stress on the power level control and spectral purity, while the harmonic conversion can complicate the receiver linearity and noise performance relative to those attributes at lower frequencies. But what impact will issues such as these have on measurements and, specifically, on extracted device models? It may help motivate the need to study such effects by considering a relatively simple example.

Consider the task of extracting the capacitance values (i.e., C_{gs} and C_{gd}) of a modern CMOS technology (i.e., with a minimum length below 40 nm) capable of reaching transit frequencies above 300 GHz, which can be computed using

$$F_T = \frac{g_m}{2\pi(c_{gs} + c_{gd})}. \tag{1}$$

Since large values of g_m in excess of 2,000 μS/μm can be achieved by using modern CMOS technologies, we can directly see that maximum transit frequencies in excess of 300 GHz can be reached when the above-mentioned capacitance levels are on the order of few femtofarads.

The characterization of such extreme impedances poses a well-known challenge due to the desensitization of reflection coefficient (Γ)to impedance (Z) [or Γ to admittance (Y)] transformations. This effect can be seen for the resistive component in Figure 2(a), where, as the reflection coefficient magnitude approaches unity, the transformation to the impedance domain (i.e., resistance) approaches an extremely low slope, resulting in a large expansion of the sensitivity to noise in the Γ measurement. Similarly, when considering a nearly ideal reactive component [Figure 2(b)], we can observe that at low (or high) capacitance

Authorized licensed use limited to: TU Delft Library. Downloaded on July 28,2026 at 14:04:21 UTC from IEEE Xplore. Restrictions apply.

values, the slope of the reflection phase also becomes progressively lower. Thus, for the small capacitances of the devices of interest for this example, relatively small errors or high noise levels in the S-parameter measurement could result in large extracted capacitance errors.

It is useful to note that the mm-wave extender architecture of Figure 1 tends to have increases in trace noise and uncertainties relative to those of the base (microwave) VNA. This is a result of the different spectral purity levels, reduced available power, and increased noise figure and conversion losses of the downconverters, with different impacts across different mm-wave bands. On average, this results in increased measurement noise, which can cause larger uncertainties in the device parameter to be extracted, due to compression in the transformation, as noted above. As an example, the trace noise characterization of a VNA-based test bench is carried out in the fundamental frequency band (i.e., 1–67 GHz) and in the WR6 (110–170-GHz) and WR3 (220–330-GHz) mm-wave bands; i.e., the test bench noise is then propagated to the measurement of an ideal 5-fF capacitor, employing an ideal calibration, where no residuals are present. The result of this analysis, which is indicative only of the noise expansion and will vary with the VNA and the extender, power level, intermediate

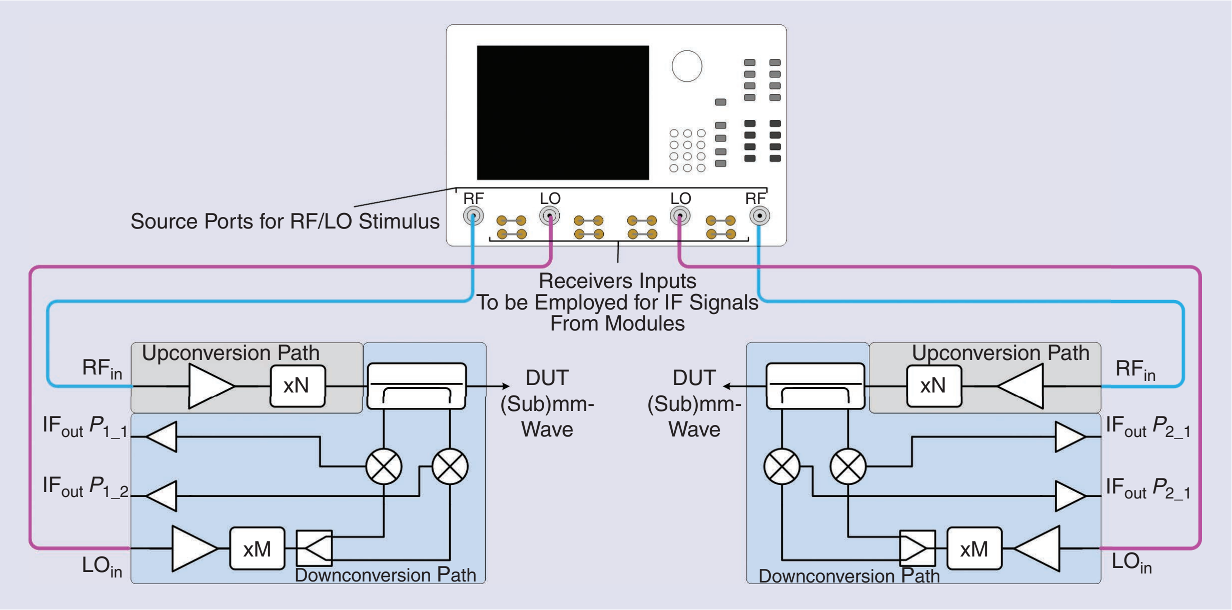

Figure 1. *A generalized vector network analyzer (VNA)-based mm-wave test-bench, employing upconverter modules to extend the main (VNA) unit frequency range. LO: local oscillator; IF: intermediate frequency.*

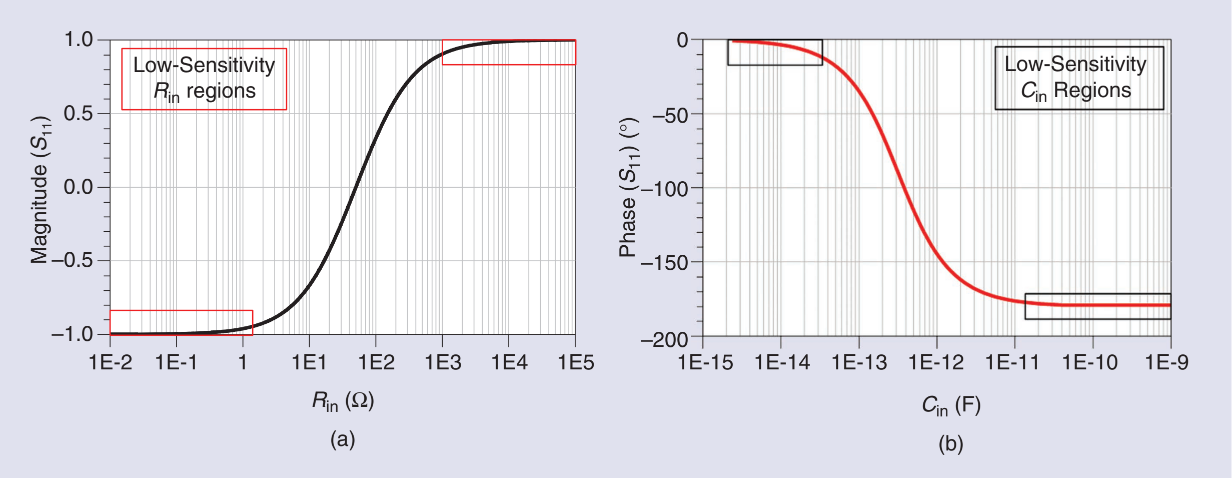

Figure 2. *The (a) magnitude (Γ)-to-real-impedance transformation and (b) phase (Γ)-to-imaginary-admittance transformation.*

Authorized licensed use limited to: TU Delft Library. Downloaded on July 28,2026 at 14:04:21 UTC from IEEE Xplore. Restrictions apply.

frequency (IF) bandwidth, and so on, is presented in Figure 3. Although the levels are not large, they do increase by nearly 10× over the 10–300-GHz frequency range.

To understand some of the mechanisms that lead to this "uncertainty" expansion, one can look at the source multiplication process. While multiplication almost always increases the phase noise (e.g., [18]) of an RF signal, the power transfer slope of multiplication can sometimes be very large. This results in amplitude noise generation as well (when not operated in saturation). This slope generally increases with the operating frequency, as the multiplier input frequency is often confined to be below ~20 GHz for practical reasons. Example plots of this conversion profile appear in Figure 4 for modules used in several waveguide bands. While one could always operate in the saturated part of this curve, this region may preclude effective power control (as will be seen), which is important for many measurement scenarios of interest in device characterization.

The higher waveguide bands are obtained by higher multiplication orders, providing an RF-to-mm-wave "gain" (decibel-milliwatts to decibel-milliwatts), with the maximum derivative going from 6.5 up to 49 in this set of curves. This translates to an increased fluctuation of both the amplitude and the phase of the upconverted wave.

Moreover, given the nonlinear nature of the multiplication architecture, the conversion tends not to be very flat with the frequency, even within a band. The net power flatness across the frequency tends to be much worse than that of the input fundamental signal unless caution is exercised. Example flatness plots for WR3 are provided in Figure 5. This unleveled flatness variation can result in trace noise variation with the frequency, as the SNR will also be changing.

The following sections look at source and receiver characteristics in more detail to get a better picture of how hardware details can affect measurements and subsequent model extractions.

Source Characteristics

In this section, we review the source characteristics in VNA-centric mm-wave test benches employed in small- and large-signal device and circuit characterization. The focus is on instantaneous power control accuracy and net spectral purity.

The instantaneous source power accuracy plays an important role in device and circuit characterization since it may trigger (when not properly implemented) both dynamic range loss and first-order (and

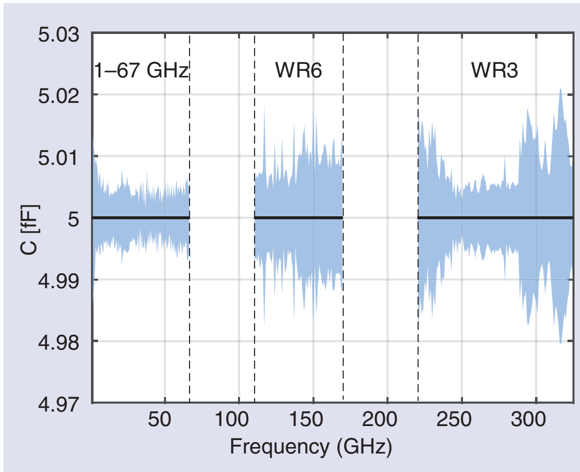

Figure 3. *The trace noise from a VNA in the fundamental band of 1–67 GHz and in mm-wave bands via extenders (WR6 and WR3) is measured and propagated through to the computation of a capacitance based on S-parameter data, using VNA tools [21]. This analysis is done for an ideal 5-fF capacitor with an ideal calibration and simply shows the effect of trace noise levels.*

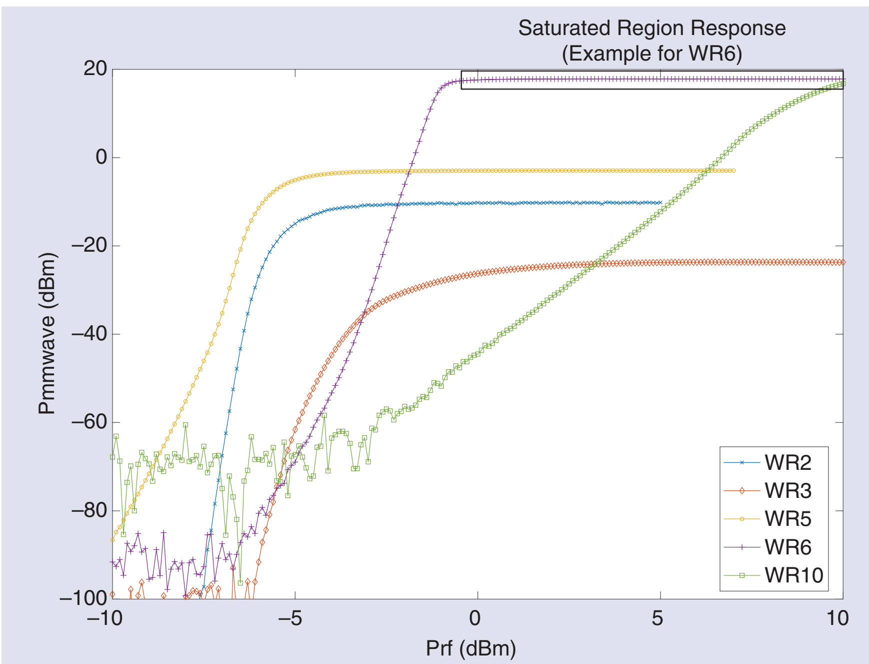

Figure 4. *Power transfer curves of source multiplication chains for several commonly used mm-wave extenders. Note the slope variations when not saturated, where Prf is the input RF power to the modules, and Pmmwave is the frequency-multiplied output RF power.*

Authorized licensed use limited to: TU Delft Library. Downloaded on July 28,2026 at 14:04:21 UTC from IEEE Xplore. Restrictions apply.

higher-order) nonlinear effects, such as amplitude modulation (AM)/AM and AM/PM (e.g., [23]).

Consider a small-signal measurement for a device where the drive power may need to be low to ensure linearity (e.g., the classical rule of thumb of a 30-dB backoff from 1-dB compression). As an example, the power-versus-frequency fluctuation of the WR3 module in Figure 5 (the red trace) would result in a loss of 11 dB of measurement dynamic range between the upper and lower parts of the band.

When a less conservative power level is used, i.e., the device is being driven close to the onset of nonlinear effects, there is a risk of inducing AM/AM distortion, transferring the nonlinear frequency tracking source characteristics to the device/circuit metrics under evaluation.

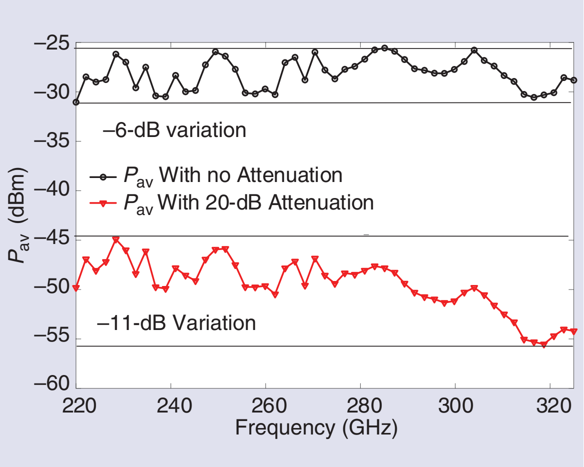

Figure 5. *The power available (Pav) variation from a frequency extender operating in the WR3 band. Without power control, this variation can map through to SNR variation.*

This effect can be seen in Figure 6(b), where the S_{21} response, measured with no power attenuation (the dashed red line), shows AM/AM distortion in the response. When the actual power level can be accurately known and the instantaneous power controlled, the frequency tracking nonlinearity can be removed, and the proper device response can be extracted [the solid trace in Figure 6(b)]. This also allows minimizing the SNR variation across the characterization band, on the (simplifying) assumption of a constant noise floor versus frequency.

A central point to the power control of the signal source is the leveling loop, which consists of some detection method within a given location in the block diagram in Figure 7, a comparison and integration block (loop amp), and a modulation block (for controlling the power).

mm-Wave direct detection has improved considerably in recent years (e.g., [24], [25], and [26]), leading to lower noise floors (minimum detectable signals), higher breakdown levels, and greater "linear" ranges. Still, the available control range of the direct detectors may be limited to ~30–40 dB, which may not be adequate for some applications (such as the small-signal device measurement discussed in the previous section).

Another approach, the heterodyne detection scheme (e.g., [23] and [27]), often converting to frequencies in the tens to hundreds of megahertz, can offer a very low-noise bandwidth. This can bring the minimum detectable signal at mm-wave frequencies to the –100-dBm range or lower with a highly linear response curve, assuming the downconverters used are linear. Such an approach exacerbates practical challenges in implementing the leveling loop. An extra (heterodyne) receiver is possible but results in an expensive solution and is often not compatible with the conventional VNAs used in mm-wave test benches. Using the test

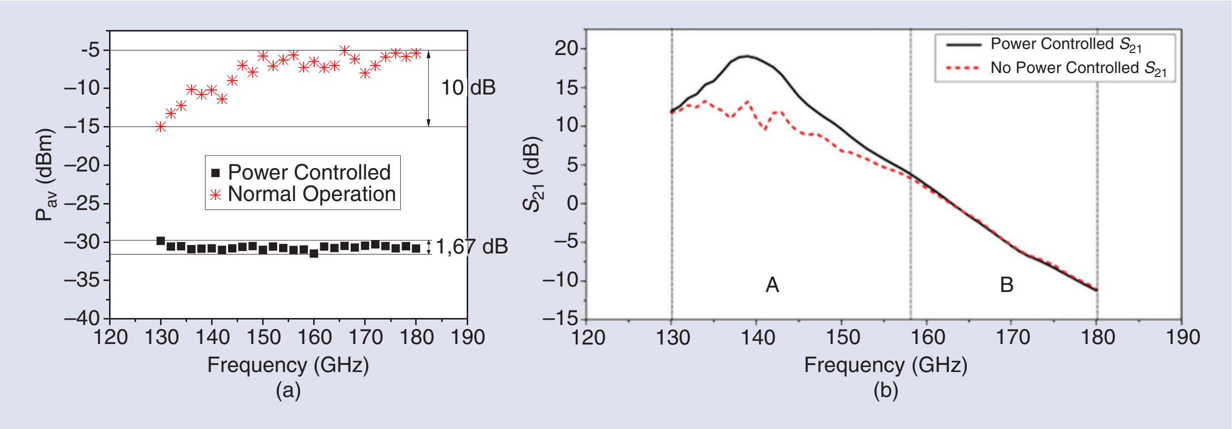

Figure 6. *(a) Power available difference between leveled (black symbols) and unleveled (red symbols) case, after the multiplication path and (b) S_{21} of the considered D-band power amplifier from [22] measured in normal (no source power control) system operation (dashed line) and with a 30-dBm controlled P_{av} (solid line).*

Authorized licensed use limited to: TU Delft Library. Downloaded on July 28,2026 at 14:04:21 UTC from IEEE Xplore. Restrictions apply.

bench's own receivers is convenient but gets complicated when measuring harmonics or other conversion products, unless multiple local oscillators (LOs) are available, as the receiver for leveling may not be tuned to the same place as the target signal. Despite the latter limitation, this is one of the solutions employed in modern VNA-centric mm-wave benches. Sensitivities and uncertainties due to the detection effects of such a method tend to be relatively constant (in decibel terms) versus the power until the levels become very low.

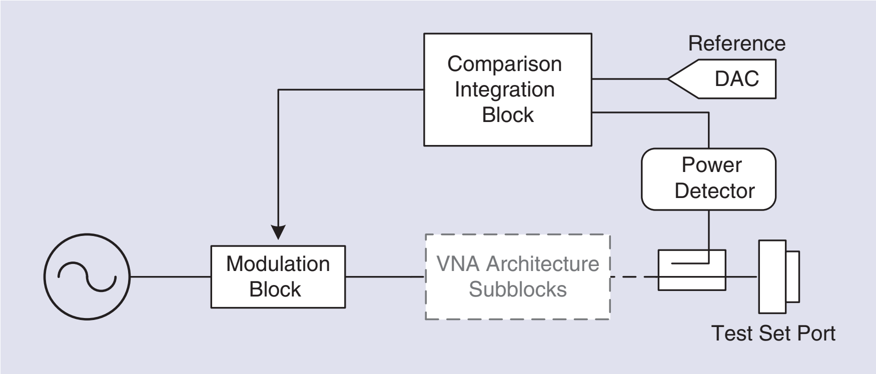

Figure 7. *A simplified leveling loop. DAC: digital-to-analog converter.*

In recent years, the comparison block section of the leveling loop has been shifting from analog to digital implementations, often allowing the use of digital correction performed as a factory calibration to achieve a constant source power level across the frequency. When considering the case of mm-wave test benches, the use of different modules, often from different vendors, makes factory calibration approaches more complicated. Moreover, given the thermal drift of the nonlinear multiplier, open-loop approaches are often not accurate enough, suggesting that module-specific calibrations for the closed-loop structure may be very useful.

After the detection and integration blocks within the loop, the gain/attenuation modulation block is the next step to realize the power control. A local mm-wave leveling loop is a possibility, and there have been recent advances in mm-wave variable-gain elements (e.g., [28]); however, as of this writing, the range and speed for a given level of insertion loss may still be limited.

Another approach is to use premultiplier modulation, as alluded to in the introduction. This task becomes more challenging as the multiplier transfer curves become steeper (see Figure 4), as the sensitivity to the control input obviously increases. If the slope is high and the loop response is not fast enough, instantaneous variations in power at 300 GHz could be on the order of multiple decibels (e.g., [23]), which could affect the linearity state of the DUT. As might be expected, the power accuracy uncertainty caused by this effect tends to be larger (in decibel terms) at lower power levels. When a premultiplier modulation is employed, a further aspect that needs to be considered is the spectral purity of the multiplied signal.

This spectral purity question is accentuated by the frequency multiplication process used in the extender modules. Given the nonlinear nature of the multiplication process, a number of harmonically related and other spurious signals will be present in the frequency band covered by the extender module, as schematically depicted in Figure 8.

When premultiplier modulation is employed, the changes in the drive level of the various stages of the multiplier result in a different level of harmonic suppression, which might lead to a drive stimulus very distant from an ideal continuous-wave (CW) excitation. In [29], a metric to identify the potential onset of these unwanted effects was found by comparing the spectral power (i.e., measured from the VNA receiver) and the total averaged power (i.e., measured from a broadband detector). This approach can help identify the power range; see Figure 9, where the premultiplier modulation can still provide a "quasi-CW" stimulus.

The plot of Figure 9 suggests how much the characteristics of the delivered power can change based on the synthesis and leveling implementation details, even when some of the gross SNR-varying behaviors and instantaneous accuracy questions have been resolved.

Receiver Characteristics

While many receiver technologies exist, the bulk of mm-wave test-bench receivers, as of this writing, use harmonic converters. This is often for reasons of the achievable LO noise performance over the needed

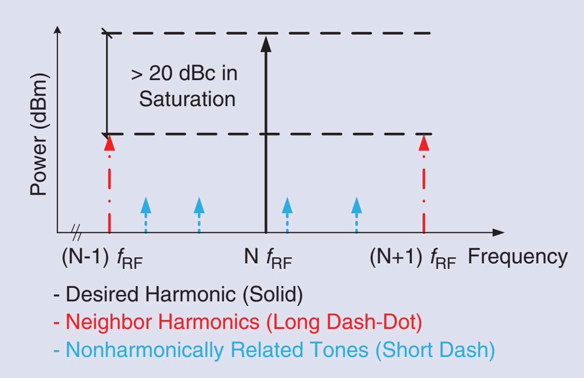

Figure 8. *The output spectral content of a mm-wave extender.*

Authorized licensed use limited to: TU Delft Library. Downloaded on July 28,2026 at 14:04:21 UTC from IEEE Xplore. Restrictions apply.

bandwidth, LO distribution complexity reasons, compatibility with current VNAs, and so on. The harmonic converter choice has implications for the receiver design in terms of spurious signal control, noise effects, and overall receiver linearity. From a practical system engineering perspective, the LO being transmitted around may be on the scale of tens of gigahertz for many of the test benches derived from commercial equipment.

Receiver IFs also vary greatly, but many are in the range of tens to hundreds of megahertz, with some upward pressure on the high end to support modulated measurements with ever-increasing communications channel widths. As this article is more concerned with model development and since current implementations using modulated signals in conventional mm-wave extenders tend to be more specialized, we do not focus on the very wide- and high-IF scenarios here.

In any measurement system looking at distortion products and device linearity parameters, the linearity of the measuring receiver itself can be important. While a common strategy is to use variable receiver attenuation, the available SNR could be limited, particularly for distortion product measurements. Such a limitation could then hinder model development in the area of low-level nonlinearities. Maximizing the linearity of the receiver is obviously as desirable as cost and complexity permit, and many authors have commented on basic receiver technologies that may help in this aspect (e.g., [30] and [31]). Certainly, front-end amplifier characteristics come to mind first.

To explore some dependencies, linearity measurement examples may help. While many receiver linearity metrics are used, a more nuanced desense measurement (where the effect of some other variable tone on the compression characteristics of the main signal is studied) may be useful. The other variable signal may be one of the spurious tones discussed in the previous section or may be a part of some more complex signaling arrangement. Desense is, of course, not a new concept, as lower-frequency receivers have been characterized with such a metric for many years [31]; however, the dependencies can be more nuanced in a mm-wave harmonic converter. Here, we interpret the term loosely in terms of the relative signal amplitudes. Consider a mm-wave WR6 system excited by two stimulus signals with independent amplitudes. In certain multitoned variants of this test (which can be useful in identifying a variety of nonlinear mechanisms and dependencies [32]), phase control between the stimulus sources is also very important in determining the net stimulus waveform to the receiver under test.

One set of data for an example system is presented in Figure 10, operating at 170 GHz using a harmonic converter. This system, at least in terms of its own compression, appears to have reasonable linearity (0.1-dB compression at 10 dBm).

One can observe a change in the onset and rate of compression with different interferer/spurious levels, as might be expected and may be another reason to monitor test conditions and the spurious signal content discussed previously. There is often a dependence on the interferer spectral content, as the peak RF amplitude statistics can vary. If there is a nonlinear contribution from the receiver IF system, that dependence on the interferer/spurious signal can become much more complicated, as mix products may land in the IF bandwidth. At the highest signal power levels, a second nonlinear mechanism is visible for this system (this one centered in the IF section), which adds some additional uncertainty.

While the receiver architecture plays a large role in behavior, the LO waveform supplied to the module can also be important. The phase noise content of the LO will often affect the noise floor and trace noise attributes, but the base LO harmonic content can also affect the conversion efficiency and linearity (e.g., [33] and [34]). As an experiment, the LO waveform is modified (but the average power and frequency are not changed) to study linearity changes. In this case, the phase of an injected third-harmonic signal (fixed

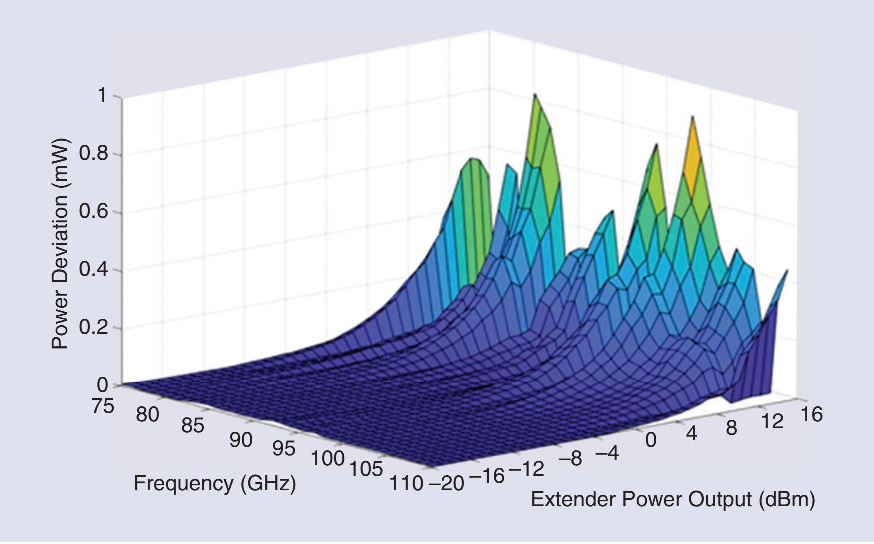

Figure 9. *The difference between the fundamental power and integrated power for an example mm-wave extender for various output levels. As the spurious content changes with the drive level, the difference between these two power quantities changes as well [29].*

Authorized licensed use limited to: TU Delft Library. Downloaded on July 28,2026 at 14:04:21 UTC from IEEE Xplore. Restrictions apply.

amplitude) is adjusted to obtain maximally and minimally linear behavior (as measured with the desense metric). The differences between the two desense responses are shown in Figure 11. The largest differences are, unsurprisingly perhaps, at the highest signal and interferer amplitudes. Interestingly, there is a small negative dip (at low interferer levels) that could be described as gain expansion. It is believed that this is due to the peak signal power itself overcoming a small LO starvation effect at this particular frequency. This type of effect would be less likely to be visible on a module with a heavily compressed LO amplifier chain, but it does point to the possibility of the drive waveform details affecting the overall linearity.

The distribution of the final LO spurious content can be related to the input content and could be changed if the LO chain was significantly overdriven. The mechanisms can become quite complex, including spectral component reconversions, frequency-dependent compression of drive amplifiers, and so on. As an example, the compression of a 330-GHz receiver is assessed for a nominal LO drive level along with two higher LO power levels that would assuredly heavily compress the LO chain, and the results are given in Figure 12. In the nominal case, the response is relatively flat (within repeatability), indicating no significant compression in this power range. The other response curves show a nonclassical compression shape that would induce added uncertainties. The highest LO level even shows a conversion shift at the lowest RF levels.

The general observation from this section, aside from the measuring receiver having finite linearity that must be balanced against the required SNR, is that the LO signal content at the converting element and even at the premultiplied input can affect that linearity.

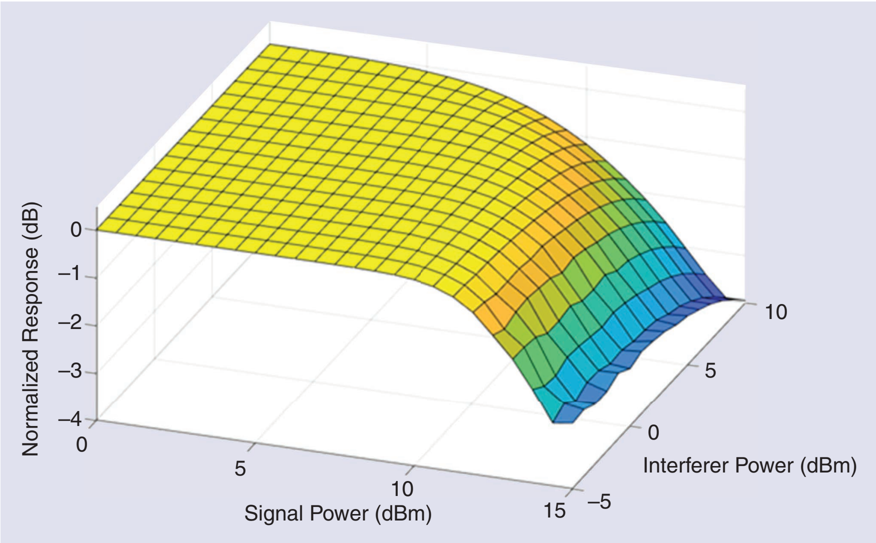

Figure 10. *Desense data for an exemplary VNA + frequency extender system, where the interferer (potentially a spurious signal) is in band but of independent amplitude. The coupling is asymmetric, and the axis labels are based on the input levels rather than the delivered levels.*

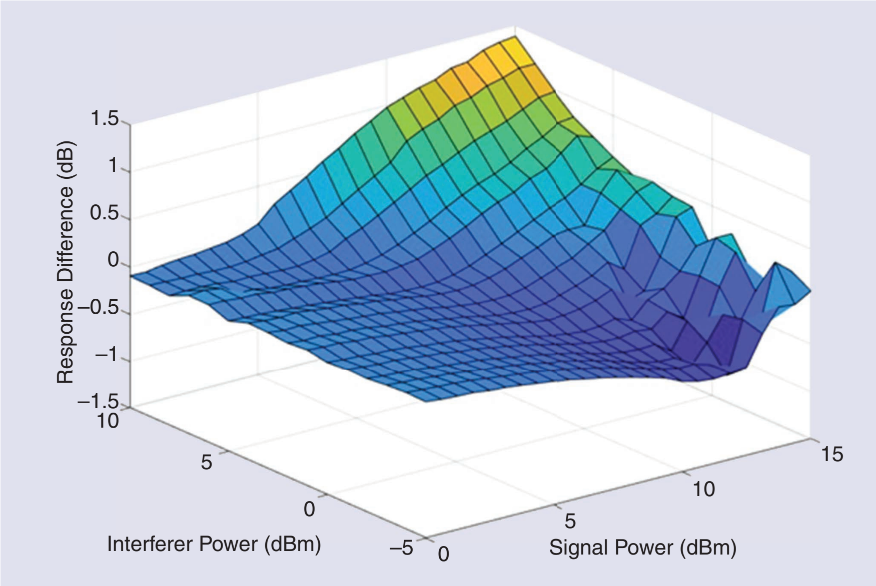

Figure 11. *The difference in the desense response as the input LO waveform in the measuring receiver is changed.*

Model Extraction Implications and Examples

In the previous sections, characteristics of the power and spectral content of the source as well as the receiver (non)linearities have been explored at higher frequencies. It has been pointed out how specific measurement parameters can be affected by these performance attributes, but the effect on the final processed data may be more complicated. Some examples may help illustrate common trends observed in practice.

Consider a purely small-signal measurement where the DUT is well out of compression. One source

Authorized licensed use limited to: TU Delft Library. Downloaded on July 28,2026 at 14:04:21 UTC from IEEE Xplore. Restrictions apply.

behavior (as discussed above) may include the presence of elevated harmonic content. Depending on the circumstances (and the DUT passband behavior), these harmonics can reconvert to the fundamental band in the instrument receiver, resulting in apparently elevated trace noise. An elevated second-harmonic (mixing with the fundamental to generate a differently phased fundamental) is one example but is less likely to happen with banded mm-wave structures. A combination of 2/3 and 4/3 harmonics (relative to the desired frequency) is one that might be possible, as would be other fractional combinations dependent on the source multiplication structure. An example of such a trace noise distribution is in Figure 13 for a nominal drive harmonic level as well as one for elevated fractional harmonics at the upper end of the band (around –10 dBc) created via a hardware modification. The trace noise increases by about a factor of two in decibel terms, but, for an example Y-parameter conversion, the scatter in the imaginary part increases by nearly an order of magnitude (in linear terms). This is partly a side effect of decibel representations and the nature of the transform, but it does illustrate a not uncommon situation.

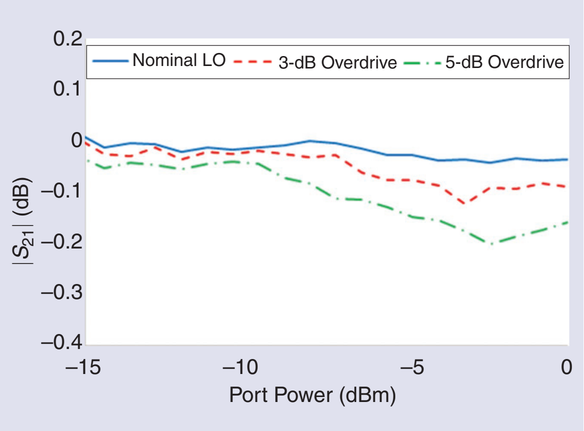

Figure 12. *The effect of significant LO chain distortion on receiver compression for an exemplary 330-GHz system.*

The magnitude of this effect relative to other uncertainty mechanisms is an important aspect to consider, even given the fact that the relative noise source contribution to the overall uncertainty tends to vary across the frequency bands.

To illustrate the latter, consider the example of on-wafer device transconductance (g_m) characterization where the device parameter is extracted in the range from 1 to 325 GHz. Note, the g_m value used in the following figures is normalized to its dc value (g_{m0}) for simplicity.

For this discussion, we consider and propagate over a realistic systematic test bench response, resulting in the following contributions: the VNA receiver noise/distortion, the probe misplacement variation, and the residual error arising from an on-wafer calibration. The calculations are not meant to represent the best possible, or even optimized, uncertainties but, rather, some typical values that could be obtained in practice.

For this, we consider an active device realized in a state-of-the-art CMOS technology, presenting $f_t/f_{\max}$ capability well above 300 GHz. The instrument noise/distortion can be propagated across the various frequency bands, as previously discussed and shown in Figure 3, employing uncertainty propagation tools as VNA tools [21].

The instrument noise is propagated to the two-port S-parameters of the DUT, and then the device metric g_m is computed and plotted in Figure 14(a). The same parameter is in Figure 14(b), renormalized on a frequency-by-frequency basis to better visualize the (small) impact of the noise contribution on the parameter uncertainty. The scale of this effect is fairly small on

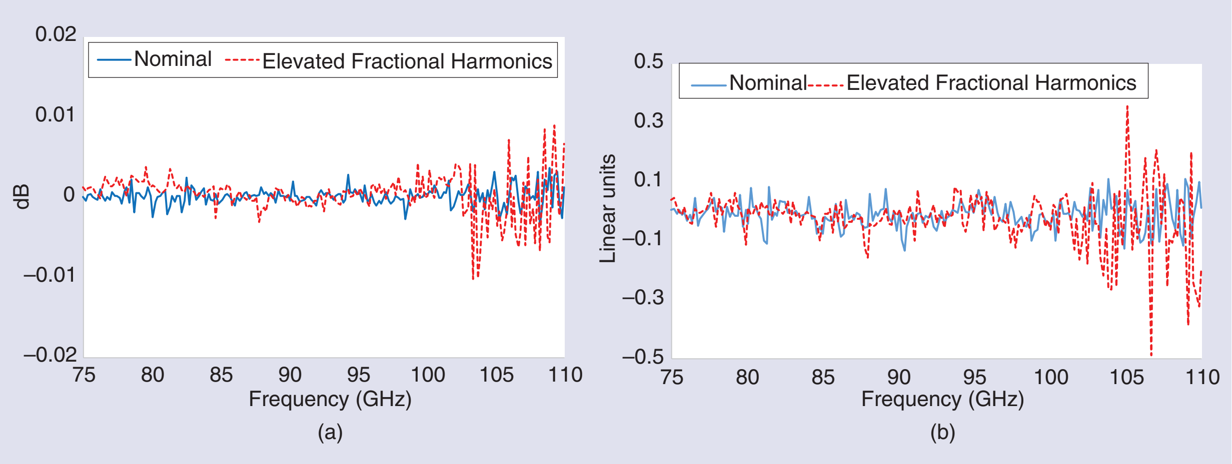

Figure 13. *(a) The possible effect of elevated source harmonics (and remixing) on an S-parameter measurement (normalized $|S_{11}|$) and (b) an extracted Y-parameter (Im (Y_{11})) for the measurement of a short circuit.*

Authorized licensed use limited to: TU Delft Library. Downloaded on July 28,2026 at 14:04:21 UTC from IEEE Xplore. Restrictions apply.

the S-parameters themselves, but this is a case where the data processing further reduced the effect.

Probe placement uncertainty has been considered extensively (e.g., [35] and [36]) and has been shown to be a critical factor in on-wafer mm-wave characterization. To analyze its relative weight in the proposed example, probe placement effects are extracted using Monte Carlo perturbations on the 2D electromagnetic (EM) models of the devices employed in the calibration process. A through-reflect-line (TRL) calibration (e.g., [37] and the references therein) on a fused silica substrate is considered, and the various EM models of devices (through, reflect, and line) are simulated using the port position (i.e., representing the probe landing position) as a parameter. The computations are performed by varying the position over circles centered on the nominal probe position, while the equivalent probe pitch (distance to the ground references ports) is kept constant [see the inset in Figure 15(a)].

The parametric model is then employed in a circuit simulation environment (i.e., Keysight ADS) to perform a Monte Carlo analysis. The port position is the perturbation, and is defined by a Gaussian random variable with a standard deviation of 2.5 μm. The results of this analysis are provided for the device g_m in Figure 15(b). The increase in sensitivity with frequency is obvious and has been commented on in the literature [35].

Finally, to include the uncertainty generated from the calibration artifacts themselves, we employ an approach similar to the one presented in [38], where EM simulations (i.e., using Keysight Momentum) are used to predict the quality of the calibration procedure given typical standard nonidealities. The materials and dimensions of the thin-film layers are considered as the potential variables.

To compute the calibration residuals, a TRL calibration kit is mapped in a circuit simulator environment (i.e., Keysight ADS) by employing the model from [39] to map the response of the grounded coplanar waveguide lines. The model is based on spectral-domain variational approaches and provides an analytical expression for the impedance and the effective permittivity of grounded coplanar waveguides. Such a line topology is often integrated in integrated circuit technology for device characterization [40], [41].

The following parameters are then perturbed in a Monte Carlo simulation based on Gaussian distributions about the nominal values:

- *Height of dielectric*: $\sigma = \pm 2.5\%$; nominal value: 8 μm
- *Permittivity of dielectric*: $\sigma = \pm 5\%$; nominal value: 4.1 μm
- *Thickness of thin-film line*: $\sigma = \pm 5\%$; nominal value: 2 μm
- *Conductivity of thin-film line*: $\sigma = \pm 1\%$; nominal value: 2.9 10^7 S/m.

It is important to emphasize that this is not intended to be a "complete" definition of the residual calibration uncertainty but, rather, to establish a reasonable bound to help with assessing relative overall uncertainty contributions. The impact of the calibration residual errors is then mapped onto the g_m of the device in Figure 16. Interestingly, the impact on g_m is greater at lower frequencies even though the absolute S-parameter uncertainties are lower there. This is a result of the nonlinear transformation to g_m (based on Y-parameters) as the input, and the output reflections

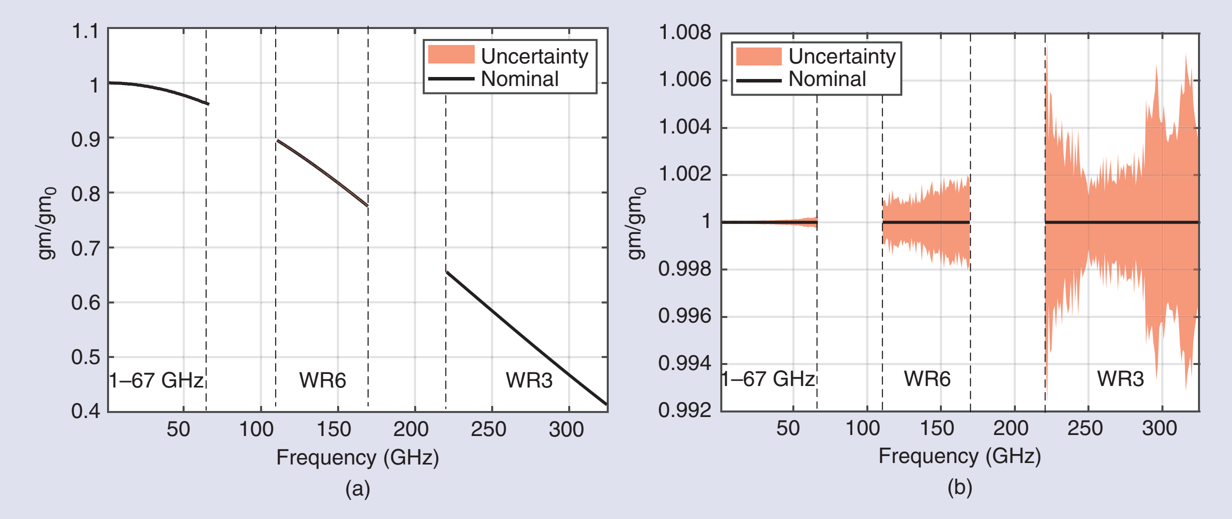

Figure 14. *(a) The normalized transconductance (normalized to its value at 1 GHz, i.e., gm_0) is used to present the (small) contributions of trace noise and instrument distortion in image. (b) A zoomed-in view using a further renormalization of the mean value at every frequency point.*

Authorized licensed use limited to: TU Delft Library. Downloaded on July 28,2026 at 14:04:21 UTC from IEEE Xplore. Restrictions apply.

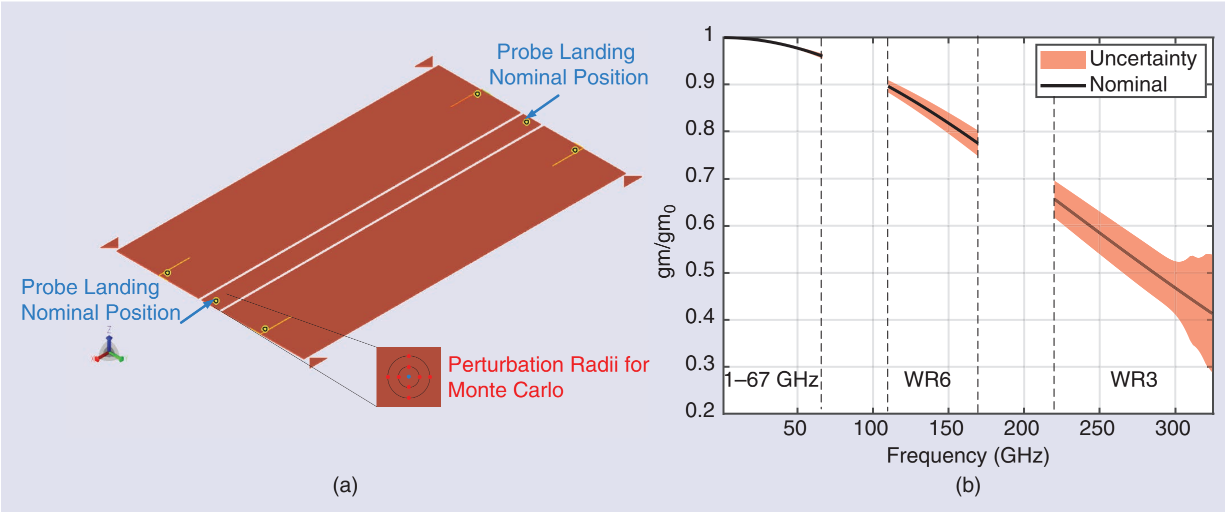

Figure 15. *The effect of probe placement, where the probe center contact is randomly placed in a (a) circular region for (b) each calibration step and the net effect computed.*

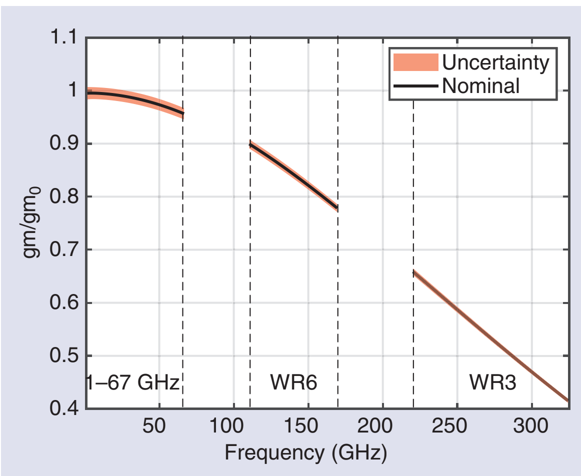

Figure 16. *The uncertainty in the measured (normalized) g_m caused by calibration residuals (Monte Carlo simulation of material and dimensional properties of on-wafer calibration standards).*

from the device are closer to the unity magnitude at low frequency (i.e., higher than 0.98 in magnitude) and decrease at higher frequencies (i.e., close to 0.5 in the WR3 band).

The relative contribution of the different error sources can be then compared at 30, 165, and 300 GHz (representative points in the frequency range used), as in Table 1. The weighting shifts dramatically to the probe placement at high frequencies, where a fixed placement error is much larger in wavelength terms. At low frequencies, the sensitivities of the postprocessing calculation accentuate the importance of the calibration residuals. Instrumentation trace noise/distortion is not a large contributor in this example, but its effect increases with the frequency. This comparison is not meant to indicate what the relative weights will always be but more to show a way to calculate an estimate and some not uncommon trends with frequency.

TABLE 1. The relative contribution of the different error sources compared at 30, 165, and 300 GHz.

Relative contribution	30 GHz	165 GHz	300 GHz
Calibration residual (%)	99.06	8.35	0.62
VNA noise (%)	0.005	0.3	0.55
Probe placement error (%)	0.935	91.35	98.83

Characterization Example

A final example is a first-order nonlinear characterization of a device (e.g., AM/AM or gain compression), and suppose that the stimulus harmonic content is not very high. If the harmonics were high, then the DUT state could interact with the drive signal in yet an additional way, and the analysis would be more complicated. The instantaneous power accuracy and its time dynamics could now be relevant since the absolute drive level is a part of the result description. Receiver linearity could also play a role depending on the absolute levels involved and the ability to buffer the receiver. The results of a Monte Carlo calculation based on experimental instrumentation and DUT characteristics are displayed in Figure 17. The random variables include a spread of the actual incident power to the DUT (based on values and mechanisms discussed previously) and a practical spread in the receiver linearity. The baseline response is shown as a thick trace. Even though the power uncertainties are much larger at lower levels (2× in decibel terms), the impact is much larger at

Authorized licensed use limited to: TU Delft Library. Downloaded on July 28,2026 at 14:04:21 UTC from IEEE Xplore. Restrictions apply.

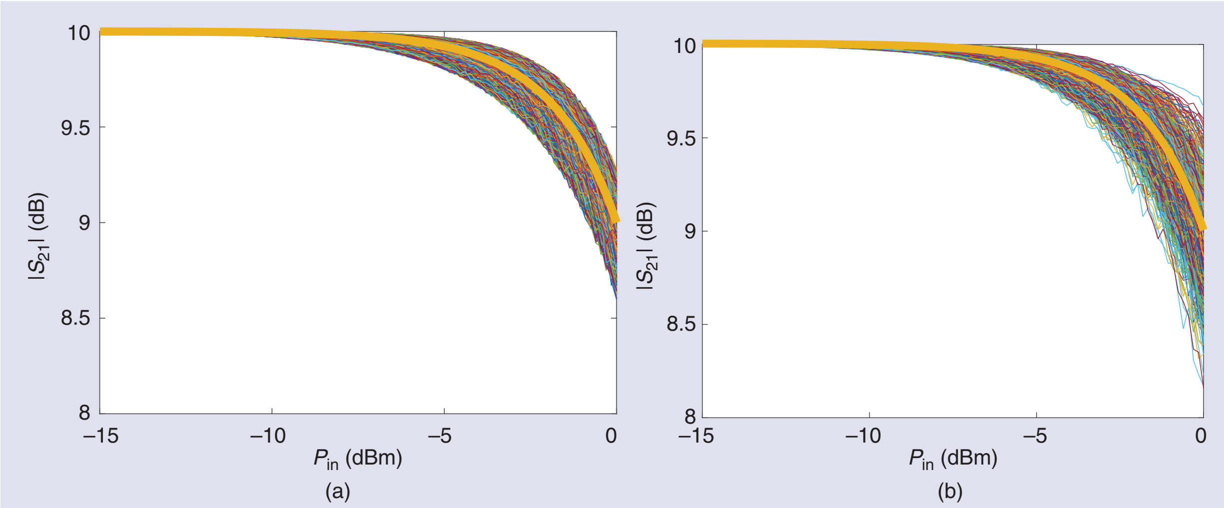

Figure 17. *(a) and (b) Monte Carlo calculations showing the effect of power uncertainty and (b) receiver compression uncertainty. The baseline DUT response is shown as a thick trace.*

higher powers, due to the DUT sensitivity. Also, the bias of the results is shifted to the more-compression side. Such a bias is common with nonlinear processes (e.g., [42]). Figure 17(b) brings in the effect of receiver compression when buffering/padding is not possible, and one can see the expected expansion at higher output levels. There is a bias to increased compression, and it may be expected, but the spread increases in both directions, as a changing DUT match interacts with the receiver in this case. While this shape change is far from universal, it does indicate one possibility where the DUT–instrumentation interaction causes a more nuanced behavior.

Again, the magnitude of these distortions relative to the increasing weight of more conventional uncertainty terms (calibration residuals, repeatability, and so on) should be assessed, and some of the effects seen in Figure 17 can be mitigated by better power control/calibration and better receiver linearity (perhaps from the receiver signal level or LO changes). For gain compression and related measurements, there is the added complication of absolute power inaccuracies being relevant (at what decibel-milliwatt power 1-dB compression happens), which has its own uncertainty framework. This topic has been well covered in the nonlinear characterization space (e.g., [43]), but it plays a role even in simple first-order measurements such as this one.

Summary

With the increasing importance of mm-wave device modeling and characterization, some instrumentation details can play a role, including drive signal purity and power accuracy as well as receiver linearity. In addition to the dependence on the specific hardware being used, the importance of the instrumentation details will vary with frequency and with how the final data are being used, as has been illustrated with some simple examples. Having a current knowledge of instrument behaviors can help in interpreting extracted model/device parameters and their sensitivities.

References

[1] M. Alsabah et al., "6G wireless communications networks: A comprehensive survey," *IEEE Access*, vol. 9, pp. 148,191–148,243, 2021, doi: 10.1109/ACCESS.2021.3124812.

[2] W. Zhang, R. Lin, and Y. Cui, "Bandwidth enhancement of a combline array antenna for mm-wave automotive radar applications," in *Proc. IEEE Conf. Antenna Meas. Appl. (CAMA)*, Guangzhou, China, 2022, pp. 1–4, doi: 10.1109/CAMA56352.2022.10002533.

[3] C. A. Lynch, A. O. Adeyeye, A. Eid, G. D. Hester, and M. M. Tenteris, "5G/mm-wave next generation RFID systems for future IoT applications," in *Proc. IEEE Intl. Conf. RFID Tech. Appl. (RFID-TA)*, Delhi, India, 2021, pp. 77–80, doi: 10.1109/RFID-TA53372.2021.9617406.

[4] W. A. Ahmad and X. Yi, "How will radar be integrated into daily life?: mm-wave radar architectures for modern daily life applications," *IEEE Microw. Mag.*, vol. 23, no. 5, pp. 30–43, May 2022. 10.1109/MMM.2022.3148343.

[5] D. Heo, "Empowering 5G and beyond: Advanced multiband signal generation and high-performance signal synthesis techniques for communications and sensing systems [From the Guest Editor's Desk]," *IEEE Microw. Mag*, vol. 24, no. 7, pp. 10–15, Jul. 2023, doi: 10.1109/MMM.2023.3264341.

[6] M. Guidy et al., "Small-signal model extraction of mm-wave N-polar GaN MISHEMT exhibiting record performance: Analysis of gain and validation by 94 GHz loadpull," in *Proc. IEEE MTT-S Int. Microw. Symp. (IMS)*, San Francisco, CA, USA, 2016, pp. 1–4, doi: 10.1109/MWSYM.2016.7540047.

[7] B. Ardouin et al., "Compact model validation strategies based on dedicated and benchmark circuit blocks for the mm-wave frequency range," in *Proc. IEEE Compound Semicond. Integr. Circuit Symp. (CSICS)*, New Orleans, LA, USA, 2015, pp. 1–4, doi: 10.1109/CSICS.2015.7314492.

[8] Q. H. Le, D. K. Huynh, D. Wang, T. Kämpfe, and M. Rudolph, "Small-signal modeling of mm- Wave MOSFET up to 110 GHz in 22nm FDSOI technology," in *Proc. IEEE Asia-Pacific Microw. Conf. (APMC)*, Singapore, 2019, pp. 222–224, doi: 10.1109/APMC46564.2019.9038620.

Authorized licensed use limited to: TU Delft Library. Downloaded on July 28,2026 at 14:04:21 UTC from IEEE Xplore. Restrictions apply.

[9] C. D. Martino, C. Esposito, M. Schroter, and M. Spirito, "Employing M1 direct calibration/de-embedding approaches for large signal model validation at mm-wave frequencies," in *Proc. 47th Int. Conf. Infrared, Millimeter Terahertz Waves (IRMMW-THz)*, Delft, Netherlands, 2022, pp. 1–2, doi: 10.1109/IRMMW-THz50927.2022.9895785.
[10] Q. H. Le, D. K. Huynh, S. Lehmann, Z. Zhao, T. Kämpfe, and M. Rudolph, "Empirical large-signal modeling of mm-wave FDSOI CMOS based on Angelov model," *IEEE Trans. Electron Devices*, vol. 68, no. 4, pp. 1446–1453, Apr. 2021, doi: 10.1109/TED.2021.3061318.
[11] V. Vadalà, A. Raffo, G. Bosi, R. Giofrè, and G. Vannini, "Advanced measurement techniques for nonlinear modelling of GaN HEMTs: From L-band to mm-wave applications," in *Proc. 15th Int. Conf. Adv. Technol., Syst. Services Telecommun. (TELSIKS)*, Nis, Serbia, 2021, pp. 63–69, doi: 10.1109/TELSIKS52058.2021.9606326.
[12] J. Wood, "A perspective on compact transistor modeling for future microwave and millimeter-wave GaN power amplifier design," in *Proc. IEEE Topical Conf. RF/Microw. Power Amplifiers Radio Wireless Appl. (PAWR)*, Anaheim, CA, USA, 2018, pp. 1–4, doi: 10.1109/PAWR.2018.8310051.
[13] G. N. Phung et al., "Influence of microwave probes on calibrated on-wafer measurements," *IEEE Trans. Microw. Theory Techn.*, vol. 67, no. 5, pp. 1892–1900, May 2019, doi: 10.1109/TMTT.2019.2903400.
[14] D. F. Williams, J.-M. Belquin, G. Dambrine, and R. Fenton, "On-wafer measurement at millimeter wave frequencies," in *Proc. IEEE MTT-S Int. Microw. Symp. Dig.*, vol. 3, San Francisco, CA, USA, 1996, pp. 1683–1686, doi: 10.1109/MWSYM.1996.512264.
[15] A. Rumiantsev, J. Martens, and S. Reyes, "Calibration, repeatability and related characteristics of on-wafer, broadband 70kHz–220 GHz single-sweep measurements," in *Proc. 95th ARFTG Microw. Meas. Conf. (ARFTG)*, Los Angeles, CA, USA, 2020, pp. 1–4, doi: 10.1109/ARFTG47271.2020.9241377.
[16] M. F. Bauwens et al., "A dual-band micromachined on-wafer probe with integrated diplexer for ultra-broadband measurements to 220 GHz," in *Proc. IEEE/MTT-S Int. Microw. Symp. (IMS)*, San Diego, CA, USA, 2023, pp. 728–731, doi: 10.1109/IMS37964.2023.10187983.
[17] M. Horibe, "Improvement of measurement uncertainty of THz waveguide vector network analyzers," in *Proc. 96th ARFTG Microw. Meas. Conf. (ARFTG)*, San Diego, CA, USA, 2021, pp. 1–4, doi: 10.1109/ARFTG49670.2021.9425171.
[18] X. Shang, "Some recent advances in measurements at millimeter-wave and terahertz frequencies: Advances in high frequency measurements," *IEEE Microw. Mag.*, vol. 25, no. 1, pp. 58–71, Jan. 2024, doi: 10.1109/MMM.2023.3321516.
[19] C. De Martino, L. Galatro, R. Romano, G. Parisi, and M. Spirito, "Hardware and software solutions for active frequency scalable (sub)mm-wave load–pull," *IEEE Trans. Microw. Theory Techn.*, vol. 68, no. 9, pp. 3769–3775, Sep. 2020, doi: 10.1109/TMTT.2020.3005178.
[20] D. Koller, S. Durant, C. Rowland, E. Bryerton, and J. Hesler, "Initial measurements with WM164 (1.1–1.5THz) VNA extenders," in *Proc. 41st Int. Conf. Infrared, Millimeter, Terahertz Waves (IRMMW-THz)*, Copenhagen, Denmark, 2016, pp. 1–2, doi: 10.1109/IRMMW-THz.2016.7758434.
[21] M. Wollensack, J. Hoffmann, J. Ruefenacht, and M. Zeier, "VNA tools II: S-parameter uncertainty calculation," in *Proc. 79th ARFTG Microw. Meas. Conf.*, Montreal, QC, Canada, 2012, pp. 1–5, doi: 10.1109/ARFTG79.2012.6291183.
[22] Z. Hu, G. Sarris, C. De Martino, M. Spirito, and E. McCune, "Design and linearity analysis of a D-band power amplifier in 0.13 µm SiGe BiCMOS technology," in *Proc. IEEE Compound Semicond. Integr. Circuit Symp. (CSICS)*, Miami, FL, USA, 2017, pp. 1–4, doi: 10.1109/CSICS.2017.8240469.
[23] J. Martens, "Improved power leveling in mm-wave/sub-THz systems," in *Proc. 42nd Eur. Microw. Conf.*, Amsterdam, Netherlands, 2012, pp. 562–565, doi: 10.23919/EuMC.2012.6459409.
[24] K. Ikamas, D. Čibiraitė, A. Lisauskas, M. Bauer, V. Krozer, and H. G. Roskos, "Broadband terahertz power detectors based on 90-nm silicon CMOS transistors with flat responsivity up to 2.2 THz," *IEEE Electron Device Lett.*, vol. 39, no. 9, pp. 1413–1416, Sep. 2018, doi: 10.1109/LED.2018.2859300.
[25] A. P. Aji, C. Apriono, and E. T. Rahardjo, "Input power and effective area in terahertz detector measurement: A review," *IEEE Access*, vol. 11, pp. 29,323–29,343, 2023, doi: 10.1109/ACCESS.2023.3260213.
[26] X. Wang, H. Cui, Y. Chen, B. Wang, W. Ma, and C. Zhang, "Fabrication, measurement and imaging demonstration of Si-based BIB terahertz array detector," in *Proc. 46th Int. Conf. Infrared, Millimeter Terahertz Waves (IRMMW-THz)*, Chengdu, China, 2021, p. 1, doi: 10.1109/IRMMW-THz50926.2021.9567604.
[27] L. Galatro, S. Galbano, A. Santaniello, and M. Spirito, "Power control for S-parameters and large signal characterization at (sub)-mmWave frequencies," in *Proc. 85th Microw. Meas. Conf. (ARFTG)*, Phoenix, AZ, USA, 2015, pp. 1–4, doi: 10.1109/ARFTG.2015.7162903.
[28] S. H. Kim, T. H. Jang, J. H. Kin, and C. S. Park, "A wideband 120-GHz variable gain amplifier with multistage phase compensation," *IEEE Trans. Microw. Theory Techn.*, vol. 68, no. 6, pp. 2419–2427, Jun. 2020, doi: 10.1109/TMTT.2020.2980518.
[29] C. D. Martino, J. Bueno Lopez, and M. Spirito, "Spectral purity evaluation of VNA frequency extenders to enable electronic software-based power control," in *Proc. 101st ARFTG Microw. Meas. Conf. (ARFTG)*, San Diego, CA, USA, 2023, pp. 1–4, doi: 10.1109/ARFTG57476.2023.10279333.
[30] V. Teppati, A. Ferrero, and M. Sayed, Eds., *Modern RF and Microwave Measurement Techniques*. Cambridge, U.K.: Cambridge Univ. Press, 2013.
[31] A. Luzzatto and G. Shirazi, "Receiving systems," in *Wireless Transceiver Design: Mastering the Design of Modern Wireless Equipment and Systems*, Hoboken, NJ, USA: Wiley, 2007, pp. 35–69.
[32] N. B. Carvalho, K. A. Remley, D. Schreurs, and K. G. Gard, "Multisine signals for wireless system test and design [Application Notes]," *IEEE Microw. Mag.*, vol. 9, no. 3, pp. 122–138, Jun. 2008, doi: 10.1109/MMM.2008.919938.
[33] F. Marki and C. Marki, "Mixers terminate intermod distortion," *Microw. RF*, vol. 48, p. 90, Dec. 2009.
[34] A. Babenko and J. Martens, "Local-oscillator third-harmonic injection for improved broadband mixer linearity," in *Proc. 99th ARFTG Microw. Meas. Conf. (ARFTG)*, Denver, CO, USA, 2022, pp. 1–5, doi: 10.1109/ARFTG54656.2022.9896519.
[35] D. F. Williams and R. B. Marks, "Calibrating on-wafer probes to the probe tips," in *Proc. 40th ARFTG Conf. Dig.*, Orlando, FL, USA, 1992, pp. 136–143, doi: 10.1109/ARFTG.1992.327008.
[36] R. Schmidt et al., "Compensating probe misplacements in on-wafer *S*-parameters measurements," *IEEE Trans. Microw. Theory Techn.*, vol. 70, no. 11, pp. 5213–5223, Nov. 2022, doi: 10.1109/TMTT.2022.3205606.
[37] U. Arz and K. Kuhlmann, "Uncertainties in coplanar waveguide and microstrip line standards for on-wafer Thru-Reflect-Line calibrations," in *Proc. 75th ARFTG Microw. Meas. Conf.*, Anaheim, CA, USA, 2010, pp. 1–5, doi: 10.1109/ARFTG.2010.5496328.
[38] C. Esposito, C. De Martino, S. Lehmann, Z. Zhao, M. Schroter, and M. Spirito, "Pre-silicon direct calibration/de-embedding evaluation and device parameters uncertainty estimation," in *Proc. 97th ARFTG Microw. Meas. Conf. (ARFTG)*, Atlanta, GA, USA, 2021, pp. 1–4, doi: 10.1109/ARFTG52261.2021.9640156.
[39] G. Ghione and C. Naldi, "Analytical formulas for coplanar lines in hybrid and monolithic MICs," *Electron. Lett.*, vol. 20, no. 4, pp. 179–181, Feb. 1984, doi: 10.1049/el:19840120.
[40] D. F. Williams et al., "Calibrations for millimeter-wave silicon transistor characterization," *IEEE Trans. Microw. Theory Techn.*, vol. 62, no. 3, pp. 658–668, Mar. 2014, doi: 10.1109/TMTT.2014.2300839.
[41] L. Galatro and M. Spirito, "Millimeter-wave on-wafer TRL calibration employing 3-D EM simulation-based characteristic impedance extraction," *IEEE Trans. Microw. Theory Techn.*, vol. 65, no. 4, pp. 1315–1323, Apr. 2017, doi: 10.1109/TMTT.2016.2609413.
[42] D. Williams, B. Jamroz, and J. Rezac, "Evaluating uncertainty of nonlinear microwave calibration models with regression residuals," *IEEE Trans. Microw. Theory Techn.*, vol. 68, no. 9, pp. 3776–3782, Sep. 2020, doi: 10.1109/TMTT.2020.3005170.
[43] P. D. Hale et al., "Traceable waveform calibration with a covariance-based uncertainty analysis," *IEEE Trans. Instrum. Meas.*, vol. 58, no. 10, pp. 3554–3568, Oct. 2009, doi: 10.1109/TIM.2009.2018012.

Authorized licensed use limited to: TU Delft Library. Downloaded on July 28,2026 at 14:04:21 UTC from IEEE Xplore. Restrictions apply.